# Post-Print of an Accepted Manuscript on the Laboratory of Turbulent Flows Website

Complete citation:

Abu Rowin, W., & Ghaemi, S. (2020). Effect of Reynolds number on turbulent channel flow over a superhydrophobic surface. *Physics of Fluids*, *32*(7), 075105. doi: 10.1063/5.0012584

The final publication is available at https://doi.org/10.1063/5.0012584



The Accepted Manuscript begins on the next page.

# Effect of Reynolds number on turbulent channel flow over a superhydrophobic surface

**Wagih Abu Rowin. Sina Ghaemi*.**
Department of Mechanical Engineering, University of Alberta, Edmonton, Alberta T6G 2G8, Canada
*Corresponding author: ghaemi@ualberta.ca

## Abstract

The slip boundary and the near-wall statistics of a fully-developed turbulent channel flow over a superhydrophobic surface (SHS) was investigated in a low Reynolds number (*Re*) range. The *Re* was varied from 6200 to 9400, based on the bulk velocity and the full-channel height. The root-mean-square of the surface roughness, normalized by the inner flow scaling, varied from 0.26 to 0.35 with increasing *Re*. Time-resolved, 2D particle tracking velocimetry (PTV) was used to obtain the mean velocity profile in the linear viscous sublayer. Further, time-resolved, 3D-PTV, was applied to obtain the Reynolds stresses. The estimated wall shear stress showed that the drag reduction of the SHS increased slightly from 37 to 42% when *Re* increased. With increasing *Re*, the slip velocity increased linearly from 0.25 to 0.34 m/s, and the slip length reduced from 97.5 to 69.6 μm. When normalized using inner scaling, slip velocity and length remained constant with increasing *Re*. The mean velocity of the SHS demonstrated a log-law with the universal von Kármán constant but shifted upward by an amount equal to the normalized slip velocity. The SHS increased the dimensional Reynolds stresses in the near-wall region and attenuated them farther away from the wall. With increasing *Re*, the differences between the dimensional Reynolds stresses of the smooth surface and the SHS increased. However, when Reynolds stresses were normalized using friction velocity, the Reynolds stresses of the SHS overlapped for all the investigated *Re* and were larger than the normalized Reynolds stresses of the smooth surface.

## 1 Introduction

Reduction of skin-friction drag can significantly reduce the energy consumption and environmental footprints of marine vessels and pipelines. It has been well known for several decades that a stable air layer over a solid surface can reduce the skin-friction drag in liquid flows (Ceccio 2010). However, only recently have superhydrophobic surfaces (SHSs) been investigated as a passive technique to reduce drag by forming an air layer at the solid-liquid interface (Rothstein 2010). This type of surface consists of nano/micro-sized asperities covered with a water-repellant coating. An SHS can hold an air layer or isolated bubbles on its surface, generating what is known as the Cassie-Baxter state (Cassie & Baxter 1944). As a result, a liquid flow can slip over the air interface, relaxing the no-slip boundary condition of solid surfaces.

Previous experiments in turbulent flows have demonstrated a large variation in SHS drag with respect to a reference no-slip smooth surface. The observations range from a similar drag (Zhao *et al*. 2007; Peguero & Breuer 2009) to a significantly smaller drag (Daniello *et al*. 2009; Park *et al*. 2014) than the no-slip surface. The variation in drag has been associated with the superhydrophobicity of the surface, the relative size of the surface asperities with respect to the length scale of the turbulent flow, and water solubility. Gose *et al.* (2018) demonstrated that SHS performance is best characterized by contact angle hysteresis at a pressure higher than the ambient pressure. 47 investigated SHSs with different surface roughness characterized using $k^+$, which is defined as the root-mean-square of surface roughness normalized by the inner length scale of the turbulent flow. They observed that SHSs with $k^+ < 0.5$ reduce drag, whereas SHSs

with larger $k^+$ increase drag. By varying water pressure in a microchannel, Dilip *et al.* (2015) controlled air solubility and therefore could control the bubble size over a hydrophobic surface. They demonstrated that change in air solubility may grow or shrink the bubbles, while the minimum surface drag is obtained when the bubbles are flush to the surface. Ling et al. (2017) and Vajdi Hokmabad & Ghaemi (2017) observed that supersaturated water increases the lifetime of the air layer, while undersaturated water increases the dissolution rate, resulting in a faster decay of the air layer. These parameters can change the morphology and thickness of the air interface, which directly affect the liquid slip over the SHS, and consequently, the drag reduction (DR) obtained using an SHS. However, if liquid slip is maintained, an SHS has the following effects on bulk properties of the turbulent flow.

It has been observed that liquid slip at the wall increases the mean velocity within the viscous and buffer layers (Abu Rowin *et al.* 2017). When the inner-layer Reynolds stresses of the turbulent flow are compared, streamwise and spanwise normal stresses of the SHS are larger than the no-slip surface, as seen by the direct numerical simulations (DNS) of Min & Kim (2004) and Rastegari & Akhavan (2015), and the experiments of Woolford *et al.* (2009) and Ling *et al.* (2016). Since the SHS has a non-permeable boundary condition, the wall-normal Reynolds stress over an SHS with low roughness has a similar magnitude as that over the no-slip surface (Min & Kim 2004; Rastegari & Akhavan 2015; Abu Rowin *et al.* 2017; Abu Rowin & Ghaemi 2019). In contrast, if an SHS has a large roughness, a higher wall-normal Reynolds stress can form as observed by Ling *et al.* (2016). Ling *et al.* (2016) and Abu Rowin *et al.* (2017) also reported a finite Reynolds shear stress at the wall, which was not observed by Rastegari & Akhavan (2015) in a DNS of turbulent flow over a flat SHS with regular patterns. The discrepancy was associated with the surface roughness in the experimental investigations of Ling *et al.* (2016) and Abu Rowin *et al.* (2017). In the outer layer, all Reynolds stress components are smaller than those over the smooth surface (Rastegari & Akhavan 2015; Abu Rowin & Ghaemi 2019), which is consistent with the reduction in turbulence over an SHS. These numerical and experimental investigations have characterized the distribution of Reynolds stresses for an SHS. However, the investigations were all carried out at a single Reynolds number, *Re*, while the effect of *Re* variation on the turbulent statistics of the flow over an SHS is not known.

There are a few experimental investigations that studied the effect of *Re* only on the magnitude of superhydrophobic DR. The experiments show two possible trends of DR increase with increasing *Re* (Jung & Bhushan 2009; Srinivasan *et al*. 2015; Daniello *et al.* 2009), and reduction of DR with increasing *Re* (Gogte *et al*. 2005; Reholon & Ghaemi 2018), depending on whether the air plastron has been maintained with increasing *Re*. Jung & Bhushan (2009) measured pressure drop in a channel flow with superhydrophobic walls at several *Re* within the laminar regime and a single turbulent *Re* of 4200 (defined based on bulk velocity and channel height). They observed a DR of 12% in the laminar regime and 30% in the turbulent regime. Srinivasan *et al*. (2015) measured the drag of an SHS in a Taylor-Couette apparatus operating in the turbulent regime. They observed 6% DR at a *Re* of $2\times10^4$ that increased to 22% at a *Re* of $8\times10^4$, where *Re* was defined based on the gap of the two cylinders and the surface velocity of the inner cylinder. For an SHS with a micro-ridge pattern, Daniello *et al.* (2009) measured negligible DR for *Re* smaller than 2500 in a turbulent channel flow. Beyond this *Re*, DR rapidly increased to 50% and was sustained up to a *Re* of 9500. In contrast, with the increase of *Re* in the laminar regime, Gogte *et al*. (2005) observed DR attenuation based on the total drag of a hydrofoil coated with a superhydrophobic layer. Aljallis *et al.* (2013) observed up to 30% DR for a superhydrophobic plate towed in a water channel compared to a control plate with no coating. However, at higher *Re* in the turbulent regime, an increase of drag was observed relative to the control plate. In the turbulent regime, Reholon & Ghaemi (2018) measured the drag of an axisymmetric model and observed a gradual reduction of DR from 36% to 6% with increasing *Re*. Their visualization of the surface showed a full air plastron at lower *Re* with DR > 16%, while the

plastron evolved into isolated menisci of air at higher *Re* with DR < 8%. In the above investigations, the variation of DR highlighted that the plastron was not fixed, and it varied across the investigated *Re* range.

To model an SHS, it is necessary to understand the variation of the slip boundary condition with *Re*, and its effect on the near-wall turbulence. Daniello *et al.* (2009) and Reholon & Ghaemi (2018) observed that increase of *Re* over SHSs increases the slip velocity, in physical units. The measurements of Reholon & Ghaemi (2018) also showed that slip length slightly reduced with increasing *Re*, as the air plastron diminished. The DNS of Martell *et al*. (2010) simulated the flow over an SHS, with alternating regions of slip and no-slip, at three $Re_\tau$ of 180, 395, and 590. With increasing *Re*, they observed that the slip velocity remained relatively constant with respect to the bulk velocity. They also found that the peaks of normalized Reynolds stresses increase and shift toward the wall with increasing of *Re*. The DNS of Lee *et al*. (2015) investigated Reynolds stresses normalized by friction velocity at three *Re* of 2800, 6785, and 10975 (based on channel half-height). At the lowest *Re* of 2800, the normalized Reynolds stresses of the inner layer for the SHS were larger than those of the no-slip surface. However, at *Re* of 6785, and 10975, the Reynolds stresses of the SHS became smaller than the no-slip surface.

Although the above numerical investigations provide valuable insight into the effect of *Re* on the turbulence over an SHS, this has yet to be experimentally evaluated to also include the effect of surface roughness and the random texture of an SHS. The previous experimental investigations of turbulent flow over an SHS by Woolford *et al.* (2009), Ling *et al*. (2017), and Abu Rowin & Ghaemi (2019) did not study the effect of *Re*. Thus, the effect of *Re* on the mean statistics and slip boundary condition over the SHSs, which feature rough and random texture, requires further experimental investigation.

We experimentally investigate the effect of *Re* on the slip boundary condition and the Reynolds stresses over an SHS installed in a turbulent channel flow. The *Re* is varied from 6200 to 9400, based on full channel height, which is equivalent to friction Reynolds numbers ranging from $Re_\tau$ = 200 to 280, based on friction velocity, $u_\tau$, and half-channel height. The SHS has a random texture structure and is fabricated using spray coating. Time-resolved, two-dimensional particle tracking velocimetry (2D-PTV) with high digital resolution is used for accurate measurement of slip velocity and length. In addition, time-resolved, three-dimensional PTV (3D-PTV) based on the shake-the-box algorithm (Schanz et al. 2016) is performed to measure near-wall Reynolds stresses. The mean velocity profile and Reynolds stresses are compared with measurements over a no-slip surface. To the authors' knowledge, this the first investigation that systematically demonstrates the effect of *Re* on turbulent channel flow developed over an SHS.

## 2 Experimental Setup

In this section, the channel flow facility, fabrication and characteristics of the SHS, and measurement systems are described. 2D-PTV measurements with high digital resolution were used to track small 5-µm polyamide tracers for estimating the slip length and velocity. This system has the advantage of obtaining the exact wall location directly from the PTV images. For measurement of Reynolds stresses, we applied a 3D-PTV based on the STB algorithm (Schanz *et al.* 2016) due to its smaller measurement noise. To mitigate the strong reflection from the rough texture of the SHSs, larger fluorescent tracers (10 µm) were used for 3D-PTV. These tracers limited the spatial resolution and rendered the 3D-PTV unsuitable for measurement in the linear viscous sublayer.

### 2.1 Turbulent channel flow

Experiments were conducted in a fully developed turbulent channel flow with a 40 mm width ($W$) and 6 mm high ($H$). The aspect ratio of $W/H$ = 6.7 is close to the recommended aspect ratio by Dean (1978) and Vinuesa *et al*. (2014) to obtain a two-dimensional flow at the centerline of the channel. To provide full

optical access, the upper and lower walls of the channel were constructed from acrylic sheets while the sidewalls were made from glass. To break down the large vortices before entering the test section, there was a settling chamber, a honeycomb, a fine mesh, and a contraction section upstream of the channel, as seen in figure 1. As observed by Dilip *et al.* (2015), high pressure leads to fast decay of the SHS plastron. Thus, the water reservoir of the flow loop was placed below the test section to decrease the test-section pressure to below atmospheric pressure. The test section was 1.2 m long and the acrylic model, with superhydrophobic coating, was installed 720 mm (120*H*) downstream of the channel entrance, flush to the upper wall. The SHS was 40 mm wide and 240 mm long, and fabricated by spray coating, which will be discussed later. An untreated acrylic surface was also used as the no-slip reference. This surface will be referred to as the smooth surface. Figure 1 also displays the coordinate system used in this study; *x*, *y*, and *z* represent the streamwise, wall-normal, and spanwise directions, respectively. The instantaneous velocity components *U*, *V*, and *W* and the velocity fluctuation components *u*, *v*, and *w* are in the *x*, *y*, and *z* directions, respectively. The velocity fluctuations are also indicated as $u_i$ in which $i$ = 1, 2, and 3 refer to *u*, *v*, and *w*, respectively.

A centrifugal pump circulated tap water in the flow loop while the volumetric flow rate was monitored using an electromagnetic flowmeter (FLR6305D, Omega Engineering, Inc., USA). The repeatability of the flow meter was estimated as ±0.01 l/s, based on different 2D-PTV experiments. A pressure transducer (P15, Validyne) with a 1.4 kPa diaphragm was used to monitor the pressure drop over the test surfaces. The uncertainty of this system was 2%, which was evaluated by repeating the pressure drop measurement over a smooth surface several times. Another pressure transducer (P15, Validyne) with a 3.5 kPa diaphragm was used to measure the test-section pressure relative to the atmosphere. The water temperature was monitored using a type-k thermocouple (TTK2425, Omega Engineering, Inc., USA), and was held constant at 23±0.5 ˚C over the course of the experiments. A program was developed in LabVIEW 2015 (National Instruments) to control the pump speed and maintain a fixed flow rate using a proportional-integral-derivative (PID) controller. The pressure transducer and the flow meter were also sampled using a data acquisition module (NI USB-6001, National Instruments). After filling the flow loop with tap water, any trapped air was removed by circulating the water for several hours. Once the trapped air was removed, and the water temperature stabilized, the SHS was installed.

Experiments over the smooth and the SHS were performed at the same flow rates. The previous investigations of Ling *et al*. (2016) and Reholon & Ghaemi (2018) observed a rapid decline of DR at high *Re*. The sudden reduction of the DR was associated with the stability of the plastron and higher diffusion of the air layer. The experiment of Ling *et al.* (2016) reported 36% DR at $Re = 20\times10^3$ while zero DR was observed at $Re = 36\times10^3$. Similarly, the DR attenuated from 23% at $Re = 5.0\times10^5$ to 1% at $1.2\times10^6$ in Reholon & Ghaemi (2018). The larger reduction of DR, suggested plastron depletion. Therefore, to investigate the effect of *Re* on a similar plastron, we maintained a relatively constant DR by considering a smaller *Re* range: five *Re* from 6,200 to 9,400 were considered. *Re* is defined here as $U_b H/\nu$, where $U_b$ is the bulk velocity (0.95 to 1.46 m/s) and $\nu$ is kinematic viscosity of water. Although the flowmeter was set at the same flow rate for the smooth and SHS tests, the 2D-PTV measurement showed a small discrepancy in $U_b$, within the repeatability of the flow meter (± 0.04 m/s in terms of $U_b$). The value of $U_b$ is estimated from 2D-PTV measurement of velocity in the upper half of the channel where SHS was installed. Therefore, *Re* over the smooth surface and the SHS will be noted by a nominal *Re*, which is shown along with the exact values in table 1. The absolute static pressure in the test section, $P_a$, is also seen in this table, which varies from 96.5 to 99.8 kPa with increasing *Re*.

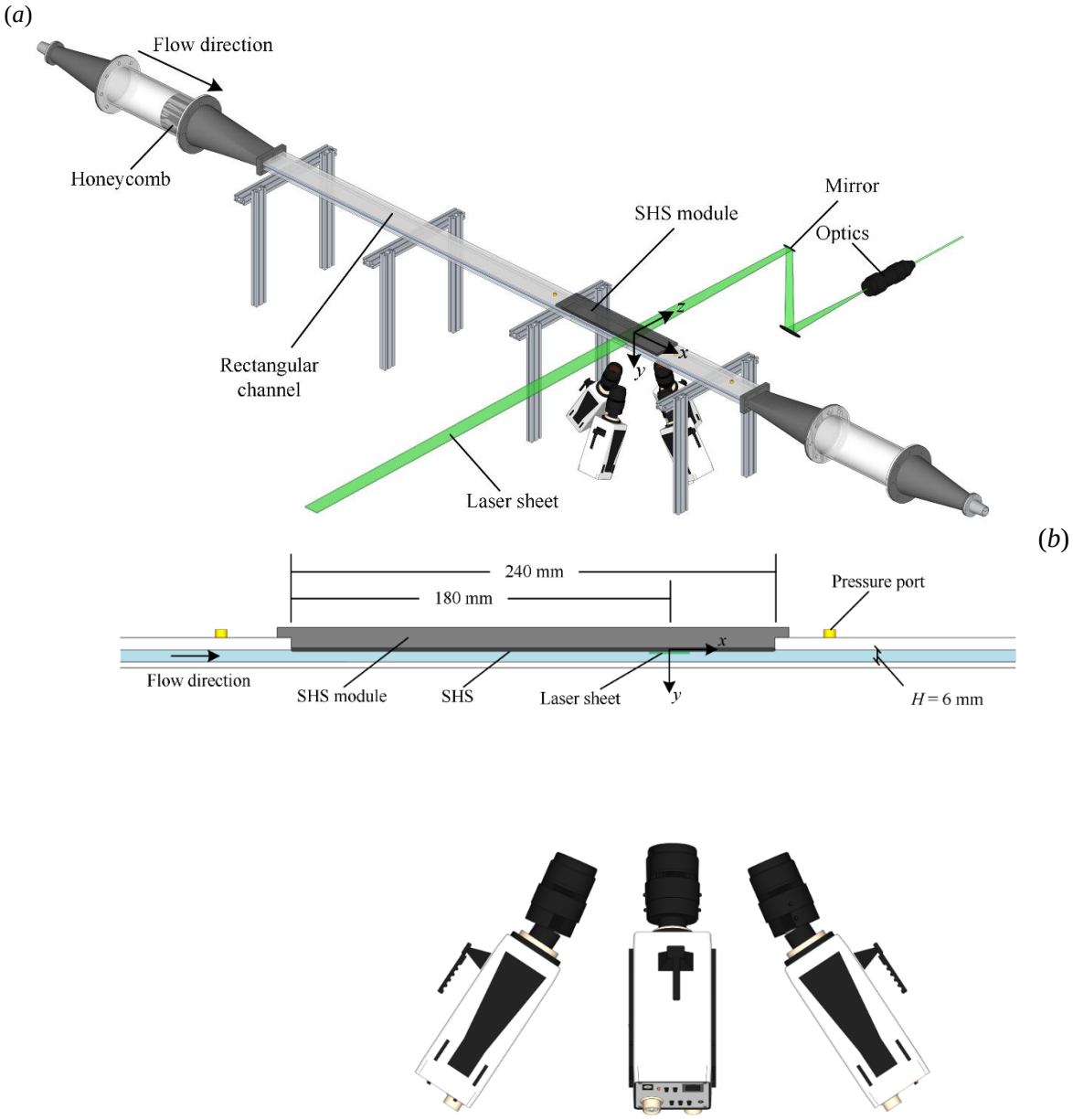


Figure 1 (*a*) Schematic of the fully developed turbulent flow facility and the 3D-PTV system. (*b*) Side view of the test section and the cameras. The fourth camera is not visible as it is located behind the middle camera.

Measurements have been carried out by a ramp-up sequence of *Re*, followed by ramp-down, over the same SHS. Both ramp-up and ramp-down phases resulted in a similar DR. This showed repeatability of the experiments, and also confirms that the air layer state is a function of test-section pressure; the air layer recovers when test section pressure is reduced by lowering *Re*.

The 2D-PTV and 3D-PTV measurements were carried out 180 mm (30*H*) downstream of transition from smooth (no-slip) to SHS and 150*H* from the channel entrance to ensure fully developed flow at the measurement location. A comparison of the time-scale of the smallest eddies and the travel time of the flow over the 30*H* distance shows that the inner layer can adapt to the new boundary condition. Based on the bulk velocity, the flow requires an advection time of 0.18 to 0.12 s to travel 180 mm for the lowest and the highest *Re*, respectively. The inner time-scale ($\lambda/u_\tau$) of the flow is 0.2 to 0.1 ms for the lowest and the

highest *Re*. Here, $\lambda$ is the viscous length, defined as $\nu/u_\tau$. Therefore, the advection time is three orders of magnitude longer than the inner time-scale of the flow. This ensures that the inner-layer adapts to the new boundary condition over the SHS.

The SHS was fabricated using a commercial superhydrophobic spray (Rust-Oleum NeverWet), which deposits two coating layers. The first layer is a silicone-based coating of methyl isobutyl ketone and butyl acetate (Liu *et al.* 2016; Gupta *et al.* 2016). This layer is hydrophilic and enhances surface adhesion before spraying the microparticles of the next layer. One pass of the silicone-based coating was applied, the surface was left to dry for about 30 minutes, and then two passes of the second coating were applied. The surface was then left for 12 hours to dry before submerging it in water. As shown in figure 2, the produced SHS has a random distribution of protrusions, which can be as large as 50 μm. The average root-mean-square height of the surface roughness, *R*, was 4.9±0.3 μm (Abu Rowin & Ghaemi 2019). The contact angle of the surface is 149±2˚ and the contact angle hysteresis is 2.8˚ measured using a droplet shape analyzer (DSA-100 KRÜSS GmbH). An estimation of the thickness of the air layer over the SHS can be roughly obtained from the height of the roughness peaks (Reholon & Ghaemi 2018; Abu Rowin & Ghaemi 2019). Reholon & Ghaemi (2018) visualized the plastron of a similar SHS in a turbulent boundary layer. Based on their observation, at the relatively large DR of the current investigation, the air-water interface is expected to be relatively flat and pinned between the largest peaks of the surface roughness. Therefore, the height of the air layer should be comparable to the largest peaks, which are about 15 μm from the profilometery of Abu Rowin & Ghaemi (2019). In the current experiment, only some of the largest roughness peaks protrude out of the plastron.

Table 1. Summary of the bulk flow parameters over the smooth and SHS.

| Nominal *Re* | 6200 | 7200 | 8000 | 8600 | 9400 |
|---|---|---|---|---|---|
| | | | Smooth surface | | |
| *Re* | 6140 | 7040 | 7880 | 8570 | 9330 |
| $U_b$ (m/s) | 0.95 | 1.10 | 1.22 | 1.33 | 1.45 |
| | | | Superhydrophobic surface | | |
| *Re* | 6230 | 7220 | 8030 | 8700 | 9380 |
| $U_b$ (m/s) | 0.97 | 1.11 | 1.25 | 1.35 | 1.46 |
| $P_a$ (kPa) | 96.5 | 97.5 | 97.8 | 98.1 | 99.8 |

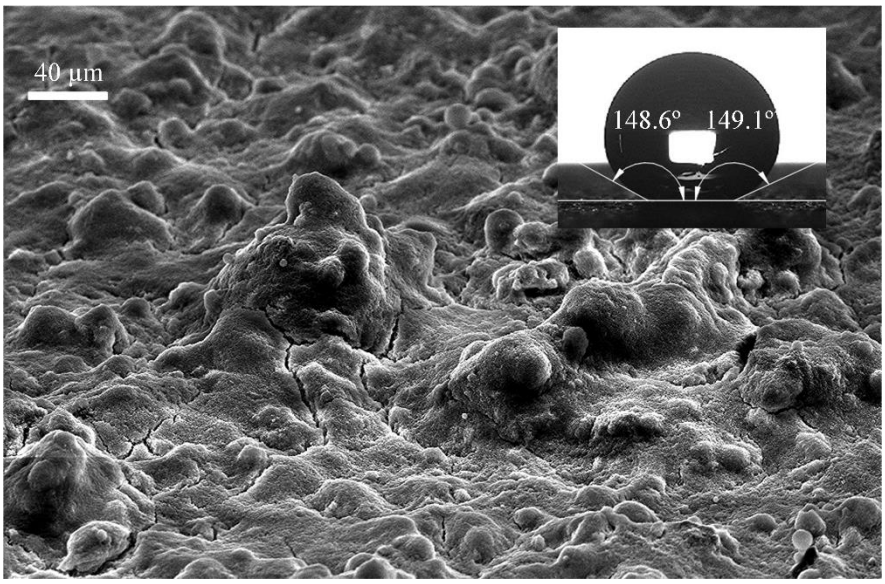

Figure 2. Micrographs of the SHS obtained using scanning electron microscopy (EVO-MA10, Zeiss microscope). The inset presents image of a water droplet on the SHS for contact angle measurement.

## 2.2 Two-dimensional particle tracking velocimetry

The flow at mid-span of the channel was characterized using high-magnification 2D-PTV measurements with a field-of-view (FOV) of 4.7×6.2 $mm^2$ in the *x*- and *y*-directions, respectively. The illumination source was a dual-cavity Nd: YLF laser (DM20-527, Photonics Industries) with 20 mJ/pulse at a wavelength of 532 nm. Using a combination of cylindrical and spherical lenses, the laser beam was shaped into a laser sheet with 1 mm thickness in the *z*-direction and 5 mm width in the *x*-direction. The flow was seeded with polyamide particles (VESTOSINT 2070) with an average diameter of 5 μm and a density of 1.016 $g/cm^3$. A high-speed Phantom v611 camera with a 1280 × 800-pixel complementary metal-oxide-semiconductor (CMOS) sensor imaged the reflected light from the tracers. Each CMOS pixel is 20 × 20 $\mu m^2$ with a 12-bit resolution. The camera was equipped with a Nikon 60-mm lens at an aperture size of $f$ / 11. The lens was connected to an 80-mm extension tube resulting in a final magnification of 2.2 and digital resolution of 8.8 μm/pixel. The laser pulses and the camera were synchronized using a high-speed controller (PTU X, LaVision, GmbH) through DaVis 8.2. Six sets of 2,048 single-frame images (12,288 images in total) were collected at a frequency of 10 kHz.

The signal-to-noise ratio of the images was improved by subtracting the minimum intensity from the ensemble of images. Following this step, the images were normalized using the average intensity of the ensemble of images and further improved using a bandwidth filter with a kernel of 3 to 7 pixels. To avoid out-of-focus particle images, particles below a specified intensity threshold and particles that were smaller than 2 pixels or larger than 6 pixels were discarded. The 2D-PTV algorithm in DaVis 8.4 was used to track the in-focus particles based on an initial velocity predictor obtained from an ensemble of correlations of the images (Meinhart *et al.* 2000). To reduce the random noise of the particle position, a second-order polynomial with a constant kernel size of 20-time steps was applied.

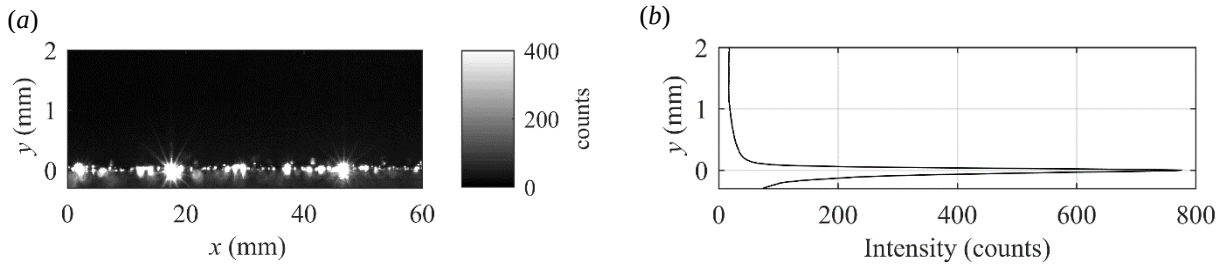


Figure 3 (*a*) Average of PTV images showing the region near the SHS. The glare line is due to reflection of the laser sheet from the SHS. (*b*) The intensity profile after averaging the image in the *x*-direction.

The accuracy of the estimated wall location in PTV images is the main source of uncertainty in calculating the inner scaling, slip length, and slip velocity of the SHS. To estimate the wall location, the glaring line, formed by the reflection of the laser light, is averaged over all the images, as shown in figure 3(*a*). The image is then averaged in the *x*-direction to obtain the intensity profile of figure 3(*b*). The location of peak intensity in the wall-normal direction (*y*) is considered to be the wall location. The uncertainty of the estimated wall location from this technique is evaluated based on the radius of the intensity profile at $1/e^2$ (~13.5%) of the peak value, which is equal to ±25 μm. This method of estimating the wall location resulted in $\pm 5\times10^{-3}$ m/s uncertainty for obtaining friction velocity and ±1.3 μm for estimating the wall unit. The uncertainty of the slip velocity and slip length are also estimated as ±0.04 m/s and ±9.1 μm, respectively. Uncertainty analysis for the measurements is included in Appendix A. To obtain the mean velocity profile, the 2D-PTV results were averaged in 10-μm bins with 50% overlap in the *y*-direction. This corresponds to 0.67 to 0.94$\lambda$ (where $\lambda$ is inner length scale) for the highest and the lowest *Re*, respectively. The bins covered the full data range in the *x* direction (4.7 mm), due to the streamwise homogeneity of the fully developed flow.

### 2.3 Three-dimensional particle tracking velocimetry

For accurate measurement of all the Reynolds stress components, time-resolved 3D-PTV was carried out based on the shake-the-box (STB) algorithm developed by Schanz *et al.* (2016). Four high-speed Phantom v611 cameras were arranged in a plus-sign arrangement, as sketched in figure 1. The angle between the wall-normal axis (*y*) and the imaging axis of the cameras was between 25˚ and 30˚. Four Nikon prime lenses with focal lengths of $f$ = 105 mm at an aperture setting of $f$ / 22 were attached to the cameras using Scheimpflug adaptors. The measurement system had a magnification of 0.56 and a digital resolution of 35.5 μm/ pixel. The illumination source was provided by the dual-cavity Nd:YLF laser (DM20-527, Photonics Industries) with 20 mJ/pulse. Cylindrical lenses were used to expand and collimate the laser beam into a thick sheet. To produce a top-hat intensity profile, the lower edge of the laser sheet was cropped by a knife-edge, and the upper side of the laser sheet was cropped by the edge of the channel wall. The final laser sheet had a thickness of 1.5 mm in the *y*-direction and a 21 mm width in the streamwise (*x*) direction. The measurement domain was $21\times1.5\times21$ mm$^3$ ($3.5H\times0.25H\times3.5H$) in the *x*-, *y*-, and *z*-directions, respectively. The laser and cameras were synchronized using a high-speed controller (PTU X, LaVision, GmbH) via DaVis 8.2. Nine sets of 1,610 single-frame images were recorded at 4 kHz ($\Delta t$ = 250 μs). To filter out the reflected light from the air plastron of the SHS, red-fluorescent particles (polystyrene, PS-FluoRed-Fi225) with 10-μm diameters were used. The tracers emit light at a 607 nm wavelength when illuminated with the 530 nm green light generated by the Nd:YLF laser. Band-pass filters with wavelength limits of 545 to 800 nm were installed on the camera lenses to record only the emitted light from the fluorescent particles while filtering out the wall reflection.

To obtain a mapping function between the image planes and the 3D measurement domain, a 2D calibration plate with a grid of 2 mm-spaced holes was used. The plate was imaged at three wall-normal locations by traversing it in 1 mm increments. The initial distortion of the calibration disparity map was about 2-3 pixels, which was reduced to below 0.02 pixels using the volume self-calibration procedure (Wieneke 2008). The signal-to-noise ratio of the images was improved by first subtracting the minimum of the image ensemble from each image, followed by intensity normalization using the average image. We also applied a local intensity normalization with a kernel of 10 pixels. The calibration and STB algorithm were performed using a commercial software (DaVis 8.4, LaVision GmbH). We limited the maximum particles shift to 13 to 20 pixels, based on *Re*, and allowed a triangulation error of 0.5 pixels. Particles within a distance of one pixel were discarded to prevent any erroneous particle trajectories. An optical transfer function (OTF) was obtained as discussed by Schanz *et al*. (2012). The maximum change in the particle shift from one time instant to the next was limited to 4 pixels and 40% relative change.

To reduce the random noise, a second-order polynomial filter was applied to the time-series of particle positions. The filter utilized a variable kernel size of 60-time steps for near-wall particles and 10 time steps for particles away from the wall. A detailed description and analysis of the regression filter is available in Abu Rowin & Ghaemi (2019). To obtain statistically converged Reynolds stresses, a bin size of 80 μm was used in the *y*-direction. The bins fully extend in *x* and *z*, forming slabs with dimensions of $21\times0.08\times21$ mm$^3$ in the *x*, *y*, and *z* directions.

The wall location in the 3D-PTV measurement was estimated by reconstructing the 3D intensity distribution of the minimum image of the data set using the multiplicative algebraic reconstruction technique (MART) algorithm (Elsinga et al. 2006). Owing to laser reflection from a few fluorescent particles which are stuck to the wall, the minimum image included small glare points. The reconstructed volume was 596×66×596 pixels. The intensity distribution was averaged in the *x*- and *z*-directions to obtain the location of the peak intensity. An uncertainty analysis for this measurement technique is also included in Appendix A.

## 3 Results

The mean velocity profiles and the Reynolds stresses from 2D-PTV and 3D-PTV are investigated in this section for the five *Re*. As was explained, the smooth surface (no-slip boundary condition) and the SHS were installed at the top wall of the channel where $y = 0$. The superscript '+' represents parameters normalized by the inner scales of the corresponding surface: friction velocity ($u_\tau$) and wall unit ($\lambda$). To study the impact of *Re* change on Reynolds stresses in physical units, the data is also normalized by a common parameter, which is chosen to be the bulk velocity at the smallest $Re = 6200$. This normalization is indicated by the subscript '*b'*. The measurement uncertainties from Appendix A are shown as error bars in the figures of mean velocity and Reynolds stress profiles.

### 3.1 Measurement evaluation over the smooth surface

The 2D-PTV and 3D-PTV measurements over the smooth surface were conducted to evaluate the state of the turbulent flow at the measurement location, provide a reference for comparison with the SHS, and evaluate the accuracy of the measurements. The latter was carried out through comparison of the measurements with DNS of the turbulent channel flow by Lee & Moser (2015) at $Re_\tau = 180$. Here, $Re_\tau$ is the friction Reynolds number, defined as $Re_\tau = u_\tau(H/2)/\nu$. This DNS data was chosen because it is close to the smallest $Re_\tau$ of the current experiment.

The semi-logarithmic presentation of $u^+$ versus $y^+$ over the smooth surface from 2D-PTV is shown in figure 4(*a*). The inner variables were estimated using the Clauser method (Clauser 1956) for this figure and

confirmed by the velocity gradient, as will be discussed later. In Clauser's method, the data is fitted on the log-law, expressed as $u^+ = 1/\kappa \ln y^+ + B$, where $u^+ = \langle U \rangle / u_\tau$ is the normalized mean streamwise velocity, $\kappa = 0.41$ is the von Kármán constant, $y^+ = y / \lambda$ is the normalized distance from the wall, and $B = 5.2$ is the intercept of the logarithmic profile. Here, $\langle\ \rangle$ indicates averaging in the homogenous flow direction ($x$ and $z$) and time. From the Clauser method, the friction velocity varied from $u_\tau^* = 0.061$ to 0.086 m/s and the viscous length varied from $\lambda^* = 15.2$ to 10.9 μm. The values with superscript '*' in table 2 indicate that the parameter is obtained from the Clauser method. Figure 4(*a*) shows that the 2D-PTV data overlaps with the log-law, while the buffer and linear viscous sublayers are also resolved. The DNS of Lee & Moser (2015) is slightly larger than the 2D-PTV, but within the error bars of the measurement. The small discrepancy between 2D-PTV and DNS is mainly associated with the finite aspect ratio of the channel in the current experiment. The DNS of Lee & Moser (2015) applies a periodic boundary condition in the $z$ direction. In general, the 2D-PTV measurements are accurate down to the near-wall location of $y^+ \sim 2$ as the data overlaps with $u^+ = y^+$ profile in the linear viscous sublayer.

Table 2. A summary of the flow parameters over the smooth and SHS. The superscript '*' indicates inner scaling of the smooth surface estimated using the Clauser method. The uncertainties of the inner-scaling is estimated based on the accuracy of the wall location.

| Nominal *Re* | 6200 | 7200 | 8000 | 8600 | 9400 |
|---|---|---|---|---|---|
| | | | Smooth surface | | |
| $u_\tau^*$ (m/s) | 0.061 | 0.067 | 0.074 | 0.079 | 0.086 |
| $\lambda^*$ (μm) | 15.2 | 13.9 | 12.6 | 11.8 | 10.9 |
| $u_\tau$ (m/s) | 0.062±5e-3 | 0.069±5e-3 | 0.076±5e-3 | 0.082±5e-3 | 0.088±6e-3 |
| $\lambda$ (μm) | 15.0±1.3 | 13.5±1.1 | 12.3±0.9 | 11.4±0.7 | 10.6±0.8 |
| $\tau_w$ (Pa) | 3.83±0.62 | 4.75±0.69 | 5.76±0.76 | 6.70±0.82 | 7.72±1.10 |
| $Re_\tau$ | 200±16 | 222±16 | 245±16 | 264±16 | 283±19 |
| | | | Superhydrophobic surface | | |
| $u_\tau$ (m/s) | 0.049±4e-3 | 0.053±4e-3 | 0.059±4e-3 | 0.063±5e-3 | 0.067±5e-3 |
| $\lambda$ (μm) | 19.1±1.6 | 17.3±1.4 | 15.8±1.1 | 14.8±1.0 | 13.9±1.1 |
| $\tau_w$ (Pa) | 2.39±0.39 | 2.80±0.42 | 3.47±0.47 | 3.95±0.63 | 4.47±0.67 |
| $Re_\tau$ | 157±13 | 174±13 | 190±13 | 203±16 | 215±16 |
| $U_s$ (m/s) | 0.25±0.02 | 0.28±0.02 | 0.29±0.03 | 0.31±0.03 | 0.34± 0.04 |
| $U_s$ / $U_b$ (%) | 26 | 25 | 23 | 23 | 23 |
| $U_s$ / $u_\tau$ | 5.1±0.4 | 5.2±0.3 | 4.9±0.5 | 4.9±0.5 | 5.0±0.6 |
| $l_s$ (μm) | 97.5±8.9 | 92.2±6.3 | 77.5±8.3 | 72.1±7.6 | 69.6±9.1 |
| $l_s$ / $\lambda$ | 5.1±0.4 | 5.2±0.3 | 4.9±0.5 | 4.9±0.5 | 5.0±0.6 |
| $k^+$ | 0.26 | 0.28 | 0.31 | 0.33 | 0.35 |
| DR (%) | 38±5 | 41±4 | 40±3 | 41±3 | 42±2 |
| $DR_{dp}$ (%) | 34±6 | 36±6 | 36±6 | 38±6 | 40±6 |

The streamwise velocity profiles over the smooth surface for $Re_\tau = 200$ to 283 from the 3D-PTV measurement are shown in the semi-logarithmic axes of figure 4(*b*). The data is normalized by the inner variables previously estimated from applying the Clauser method to the 2D-PTV measurement, as it was shown in Figure 4(*a*). The data at $y^+ < 4$ are discarded due to discrepancies of the 3D-PTV results with respect to $u^+ = y^+$ of the linear viscous sublayer. The discrepancies are associated with the large size of the fluorescent tracers (10 μm) with respect to $\lambda^*$, which varies from 15.2 to 10.9 μm with increasing *Re*. Farther

away from the wall, the $u^+$ profiles coincide with the log-law until $y^+ \approx 100$, which is the upper limit of the 3D measurements.

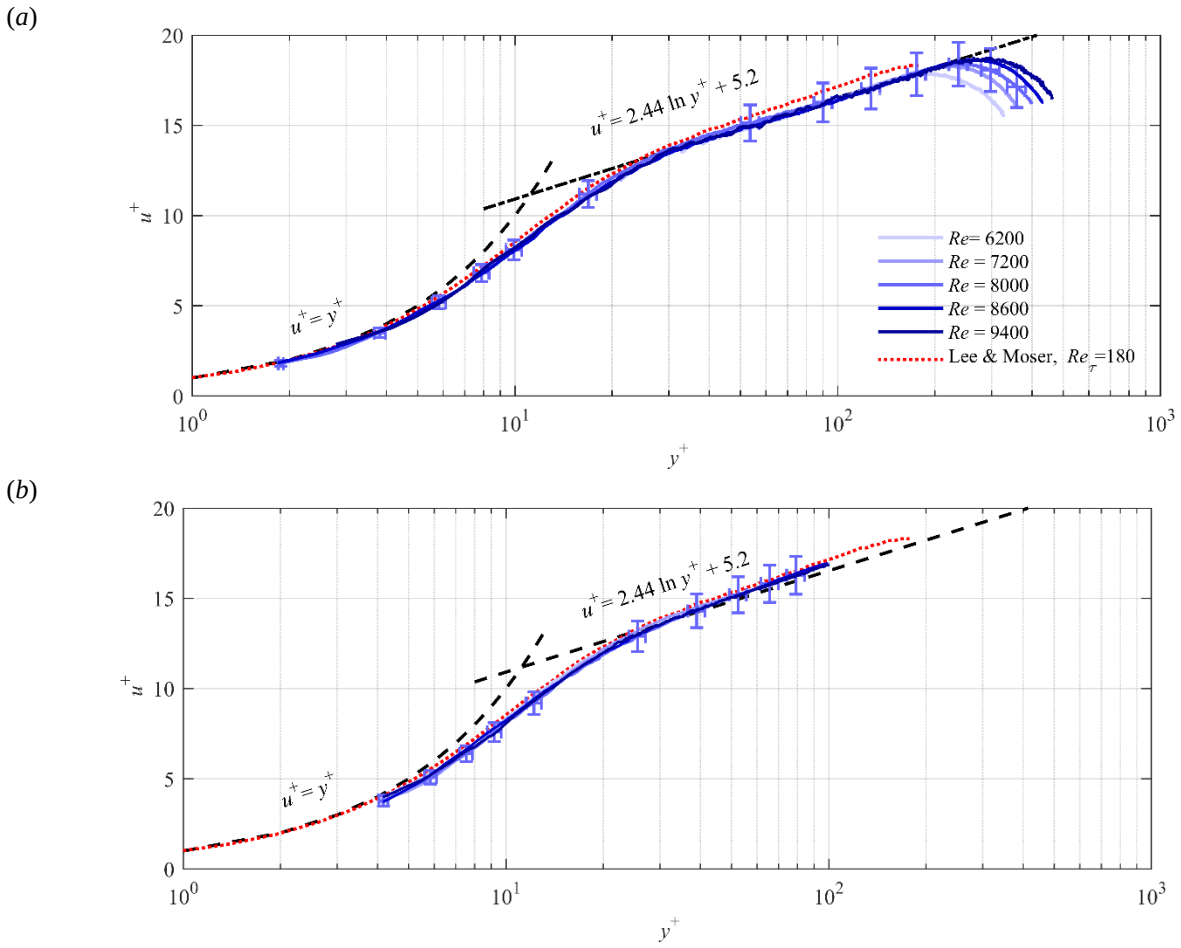


Figure 4. Semi-logarithmic presentation of the mean streamwise velocity profile over the smooth surface from (*a*) the 2D-PTV and (*b*) the 3D-PTV measurements. The data is normalized by the inner scale of each case. The error bars are only shown for *Re* = 8000 based on Appendix A.

The mean velocity at $y^+ < 20$ from 2D-PTV is plotted in linear axes in figure 5. The inner scaling used to normalize velocity and wall-normal distance in figure 5 are estimated based on the wall-normal gradient of mean velocity from 9 data points available from 2D-PTV at $2 < y^+ < 3.5$ of the linear viscous sublayer. This linear range is limited to $y^+$ of 3.5 (instead of 5) since there is about 5% deviation from the law-of-the-wall at $y^+ = 5$ (George 2013). The estimated parameters from the velocity gradient are within 4-8% of those estimated from the Clauser method in figure 4(*a*), as seen by comparison of the values in table 2. Using the velocity gradient method, the estimated friction velocity varies from $u_\tau = 0.062$ to 0.088 m/s, the viscous length from $\lambda = 15.0$ to 10.6 μm, and $Re_\tau$ from 200 to 283. In the next section, the wall-normal gradient of mean velocity will be used to estimate the inner scaling over the SHS since the Clauser method cannot be applied to a drag-reduced case. Figure 5 also illustrates that extrapolation of the linear fit approaches $u^+$=0.2 at $y^+ = 0$, which is within the estimated uncertainty of the measurement. Table 2 also shows the estimated wall shear stress, $\tau_w = \rho\, u_\tau^2$, where $\rho$ is the water density.

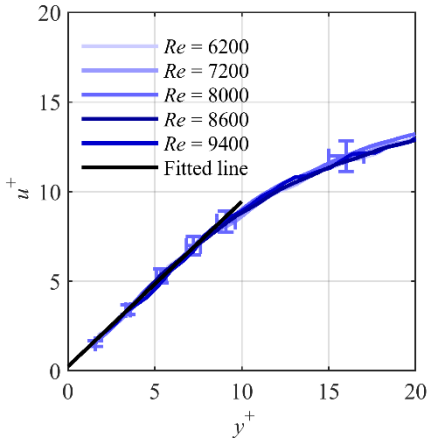


Figure 5. Mean streamwise velocity profile in the inner layer over the smooth surface from 2D-PTV.

Reynolds stresses of the turbulent channel flow over the smooth surface from 3D-PTV for the near-wall region of $y/H < 0.10$ ($y^+ < 50$) are shown in figure 6. The left-side plots of figure 6(*a*, *c*, *e*, *g*), show Reynolds stresses normalized by $U_b^2$ at $Re = 6200$ (smallest *Re*), as denoted with subscript '*b*'. The wall-normal distance is also normalized using the channel height. As expected, Reynolds stresses increase with increasing *Re*. Due to a thinner inner layer at higher *Re*, the peaks of Reynolds stresses also shift toward the wall with increasing *Re*. This is clearly seen for $\langle u^2 \rangle_b$, which peaks between $0.02 < y/H < 0.04$. The profiles of Reynolds stresses approach zero with reducing wall-normal distance, as expected for a no-slip boundary condition.

In the right-side plots of figure 6(*b*, *d*, *f*, *h*), Reynolds stresses at each *Re* are normalized by their corresponding inner scaling, $\langle u_i u_j \rangle^+ = \langle u_i u_j \rangle / u_\tau^2$. The normalization by the inner scaling results in a relative overlap of $\langle u^2 \rangle^+$, $\langle v^2 \rangle^+$, and $\langle w^2 \rangle^+$ for different *Re* with subtle inconsistencies for $y^+ > 15$. The DNS of Lee & Moser (2015) at $Re_\tau = 180$ is also presented . The measured Reynolds stresses at $Re_\tau = 200$ and 222 are comparable with the DNS profile, while the Reynolds stresses become larger than the DNS profile for the larger $Re_\tau$ cases.

### 3.2 Mean velocity over the SHS

Figure 7 presents the near-wall streamwise velocity profiles over the SHS from 2D-PTV on linear axes. The inner scales are estimated from the wall-normal gradient of mean velocity within $2 < y^+ < 3.5$ and are summarized in table 2. As can be seen from figure 7, $u^+$ profiles of the SHS at different *Re* overlap with a subtle discrepancy of at most a 6% difference at $y^+ = 16$. It is also noted that the normalized slip velocity, $u_s^+ = U_s/u_\tau$, for all *Re* tests approaches ~5.0 based on extrapolation of the linear fit to $y^+ = 0$.

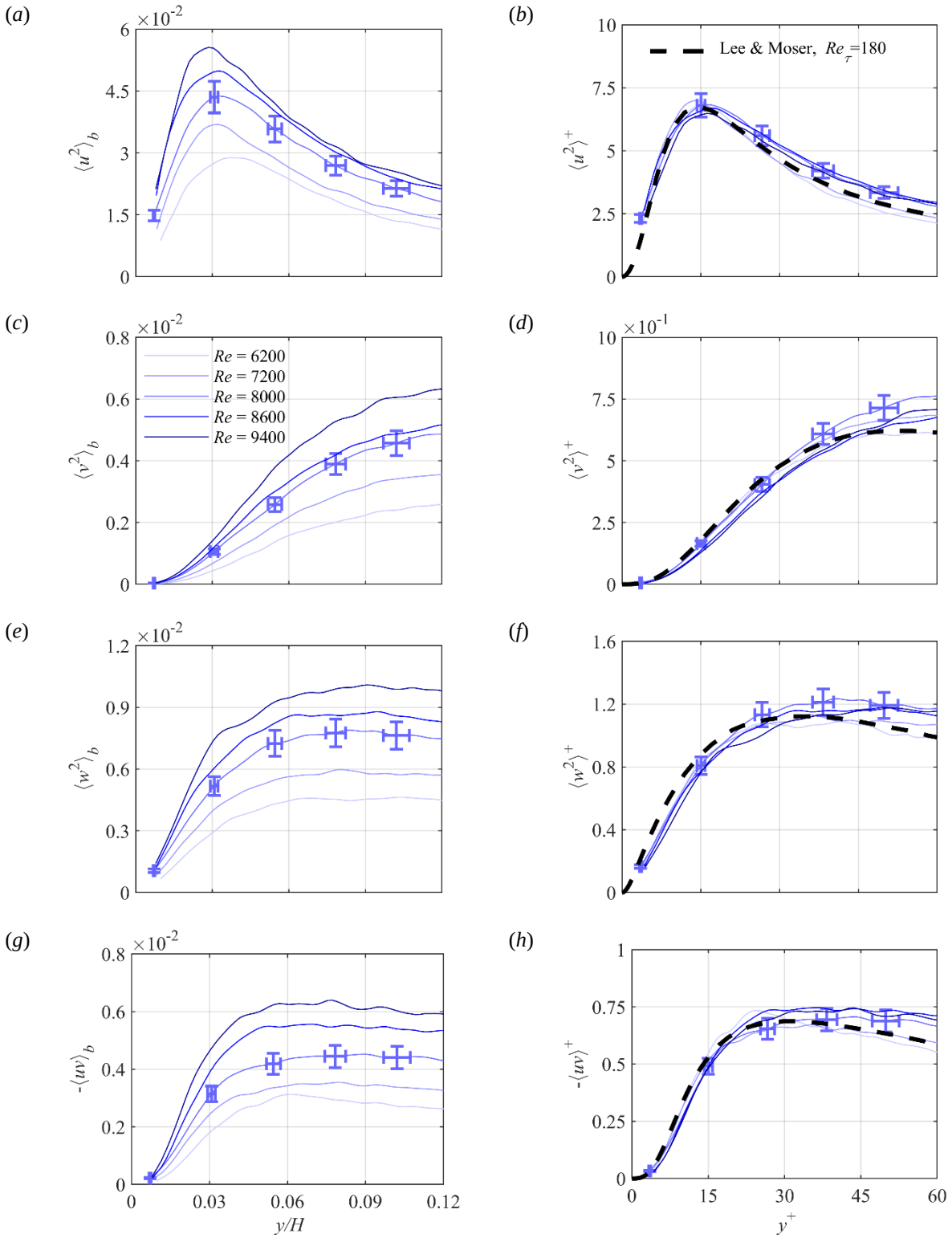


Figure 6. 3D-PTV measurement of (*a*-*b*) streamwise, (*c*-*d*) wall-normal, (*e*-*f*) spanwise and (*g*-*h*) shear Reynolds stresses over the no-slip smooth surface. The parameters of the left side plots are normalized by $U_b$ of the flow at the lowest *Re* and the channel height, while for the right-side plots, normalization using the corresponding inner scaling is applied.

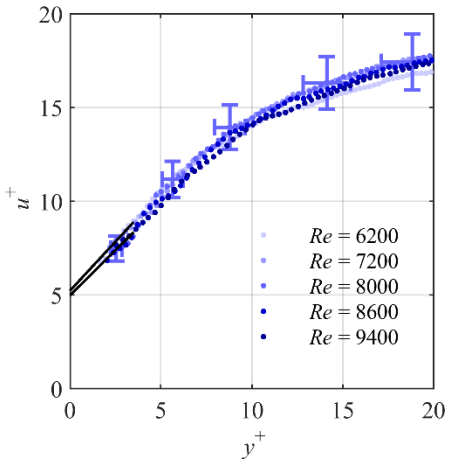


Figure 7 Mean streamwise velocity profiles over the SHS at different *Re* normalized by the corresponding inner scaling. The fitted lines are only shown for *Re* = 6200 and 9400 for clarity.

To better investigate the effect of *Re* on the slip boundary condition over the SHS, slip velocity is also investigated in physical units (m/s), as well as normalized using inner and outer scalings. A plot of $U_s$ in m/s is presented against *Re* in figure 8(*a*) and the values are also available in table 2. The error bars show the uncertainty as discussed in §2.2. Due to the larger velocity gradient at the wall, the error in estimating $U_s$ increases with *Re*. As shown in figure 8(*a*), $U_s$ gradually increases from 0.25 to 0.34 m/s with increasing *Re*. The PIV of Daniello *et al.* (2009) also observed an increase of $U_s$ over an SHS with microgrooves with increasing *Re*, although they did not provide any detail about the spatial resolution and uncertainty of their PIV. The microscopic PTV of Reholon & Ghaemi (2018) also showed a larger $U_s$ with increasing *Re* for the SHS applied on a body-of-revolution. The DNS of Lee *et al*. (2015) demonstrated the same trend of an increase of $U_s$ as *Re* increases for an SHS modeled as a surface pattern with slip and no-slip regions.

The effect of *Re* on the normalized slip velocity, $u_s^+$, is plotted in figure 8(*b*). We noticed that $u_s^+$ over the current SHS remains relatively stable at ~5.0 at different *Re*. In contrast, the DNS of Martell *et al*. (2010) reported an increase of $u_s^+$ with increasing *Re*, for a wider range of $Re_\tau$ varying from 180 to 590. Similar to Martell *et al*. (2010), Lee *et al*. (2015) modeled the SHS as an organized surface pattern with slip-free areas. They associated the increase of $u_s^+$ to the increase in the size of the micro cavities relative to the wall units. It is important to also note that, in their DNS, the SHS was assumed flat with no surface roughness. The values of $U_s$ normalized using $U_b$ are shown in table 2. It is observed that $U_s/U_b$ slightly reduces, varying from 26 to 23% with increasing *Re*. The DNS of Martell *et al*. (2010) reported a relatively constant $U_s/U_b$ for three $Re_\tau$.

In general, this evaluation shows that slip velocity (in physical units) increases with increasing *Re*. However, the measured increase of slip velocity with increasing *Re* is smaller than that observed in the previous numerical simulations. In the current experiments, $u_s^+$ was constant and $U_s/U_b$ slightly reduced with increasing *Re*. The discrepancy is associated with the assumed constant slip-free area of the numerical simulations with increasing *Re*.

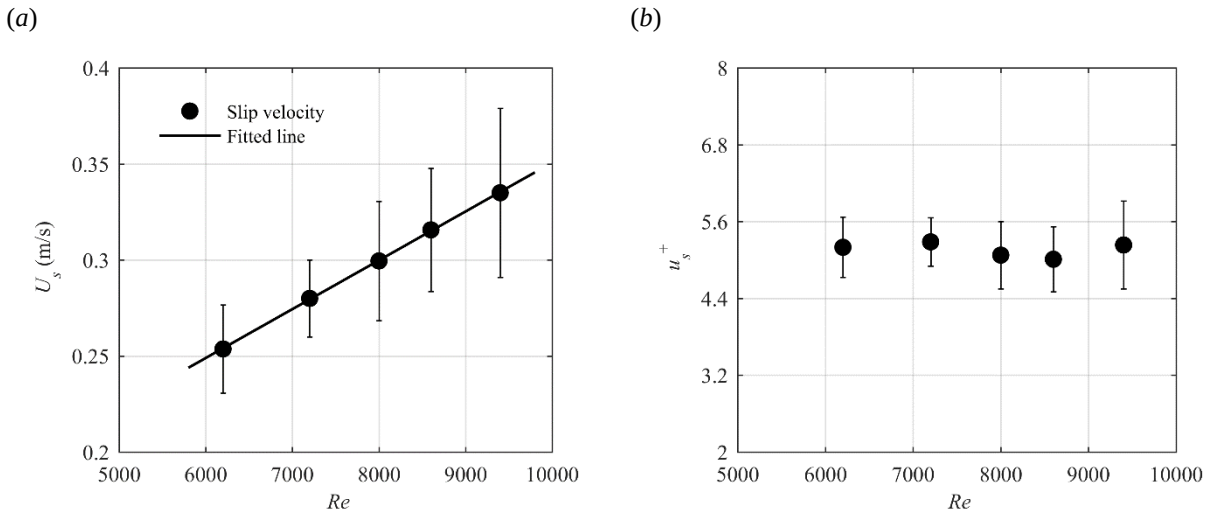


Figure 8 Slip velocity measurement over the SHS at different *Re* (*a*) in terms of m/s and (*b*) normalized by the corresponding inner scaling. The error bars represent the uncertainty in estimating the wall location from 2D-PTV.

The slip length is estimated according to $l_s = U_s\, \partial\langle U\rangle/\partial y$, where $\partial\langle U\rangle/\partial y$ is the velocity gradient at the wall. This quantity shows an imaginary distance, $l_s$, where extrapolation of $\langle U\rangle$ over SHS reaches zero. The dimensional $l_s$ is shown in figure 9(*a*) as a function of *Re*. It is observed that $l_s$ decreases from 97.5 μm at $Re$ = 6200 to 69.6 μm at $Re$ = 9400. It is conjectured that the reduction is associated with the decrease of the air plastron thickness due to an increase in test-section pressure, which increases the solubility of air in water. As Dilip *et al.* (2015) observed, an increase in the air solubility of water at higher pressures can dissolve the air layer. The shadowgraphy imaging of Reholon & Ghaemi (2018) showed that a large *Re* can accelerate plastron depletion. They observed that, at the largest considered *Re* of $1.5\times10^6$, the air plastron was depleted and the roughness features of the SHS were fully exposed to the flow. Ling et al. (2017) described a diffusion-induced wetting process due to undersaturated flow, which includes downward migration of the plastron into the SHS cavities followed by shrinkage of the bubbles.

With increasing *Re*, the normalized root-mean-square of surface roughness, $k^+ = R/\lambda$, increases from 0.26 to 0.35, as shown in figure 9(*b*). This increase of $k^+$ is accompanied by an increase of DR. Based on investigation of several SHSs with random textures, Bidkar *et al*. (2014) suggested that, to obtain a large DR, the optimum $k^+$ should be approximately 0.5. The measurements of Ling *et al.* (2016) also agreed with this observation; they observed an increase of DR from 9% to 36% as $k^+$ increased from 0.43 to 0.68. For $k^+ > 0.68$, DR started to decline until reaching a drag increase over an SHS with $k^+ = 3.28$. Reholon & Ghaemi (2018) also examined the effect of the surface roughness on the DR. When $k^+$ was larger than 0.5, they observed smaller DR with increasing $k^+$.

(*a*) (*b*)

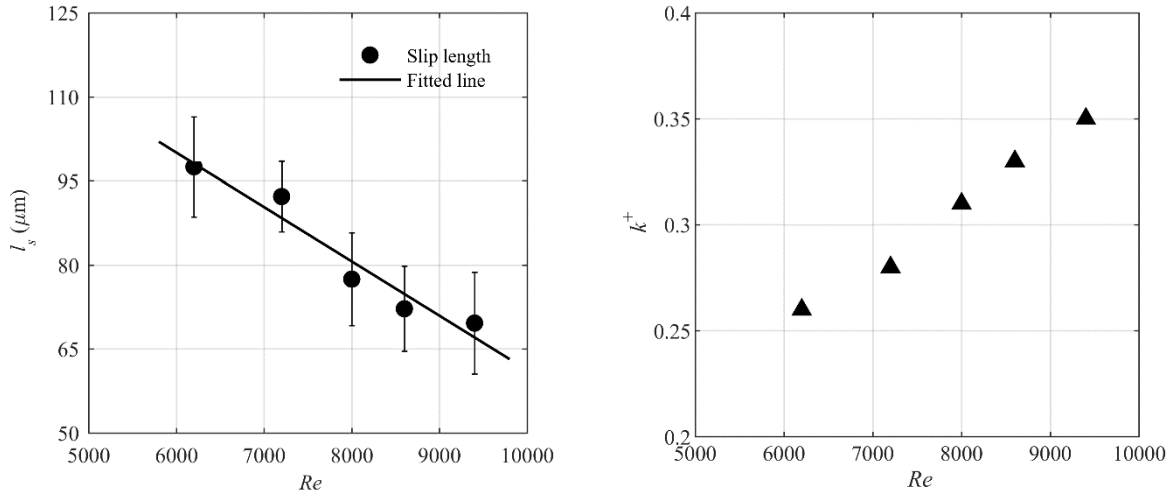


Figure 9 (a) Slip length measurements over the SHS at each *Re* in terms of μm, and (*b*) normalized surface roughness. The error bars represent the uncertainty in estimating the wall location from 2D-PTV.

The semi-logarithmic profiles of $u^+$ over the SHS from the 2D-PTV for different *Re* are presented in figure 10(*a*). As can be seen, there is an upward shift of $u^+$ for all *Re* cases when compared with the law-of-the-wall and the log-law of a smooth surface. This shift, which is due to the presence of slip velocity, was observed in the DNS of Min & Kim (2004), and also in the experiments of Ling *et al.* (2016) and Abu Rowin *et al.* (2017). The new observation from Figure 10(*a*) is that the semi-logarithmic velocity profiles of different *Re* approximately overlap, with a small upward shift with increasing *Re*. Comparison with Reholon & Ghaemi (2018) shows that the small variation is only present when variation in DR is also small. Reholon & Ghaemi (2018) observed large variation in the log-law shift at different *Re*, which was associated with the large DR variation with changing *Re*. In their investigation, the DR percentages varied from 23% to 1% as *Re* varied from $5.0 \times 10^5$ to $1.2 \times 10^6$.

Figure 10(*b*) illustrates the semi-logarithmic profiles when the slip velocity is subtracted from the mean velocity (i.e. $u^+ - u_s^+$). As can be seen, the profiles approximately overlap with the law-of-the-wall and the log-law of the smooth wall. Although, the error bars indicate the possibility of small variations within the bands of the measurement uncertainty. This observation appears to be different from the DNS of Min & Kim (2004), Rastegari & Akhavan (2015), and Busee & Sandham (2012). In these numerical investigations, the logarithmic region of $u^+ - u_s^+$ is shifted downward with respect to the log-law of a smooth surface. The discrepancy might be due to the difference in the ratio of streamwise to spanwise slip with respect to the current experiment (i.e. dominance of the streamwise slip). In addition, it is important to note that none of these numerical simulations modeled a random surface roughness. The numerical simulations also assumed a flat rigid interface and neglected any vibration of the air-liquid interface. Most of the measured velocity profiles of Ling (2017) also demonstrate a downward shift of $u^+ - u_s^+$. However, in Ling (2017), the mean velocity profile of a SHS manufactured through sandblasting agrees with the current measurements. The $u^+ - u_s^+$ profile of this surface, indicated as SB in Ling (2017), overlaps with the log-law of a smooth surface. Further investigation of $u^+ - u_s^+$ profiles for a variety of SHSs is needed to scrutinize the discrepancy. Such investigations are rare due to experimental challenges in measuring the slip velocity.

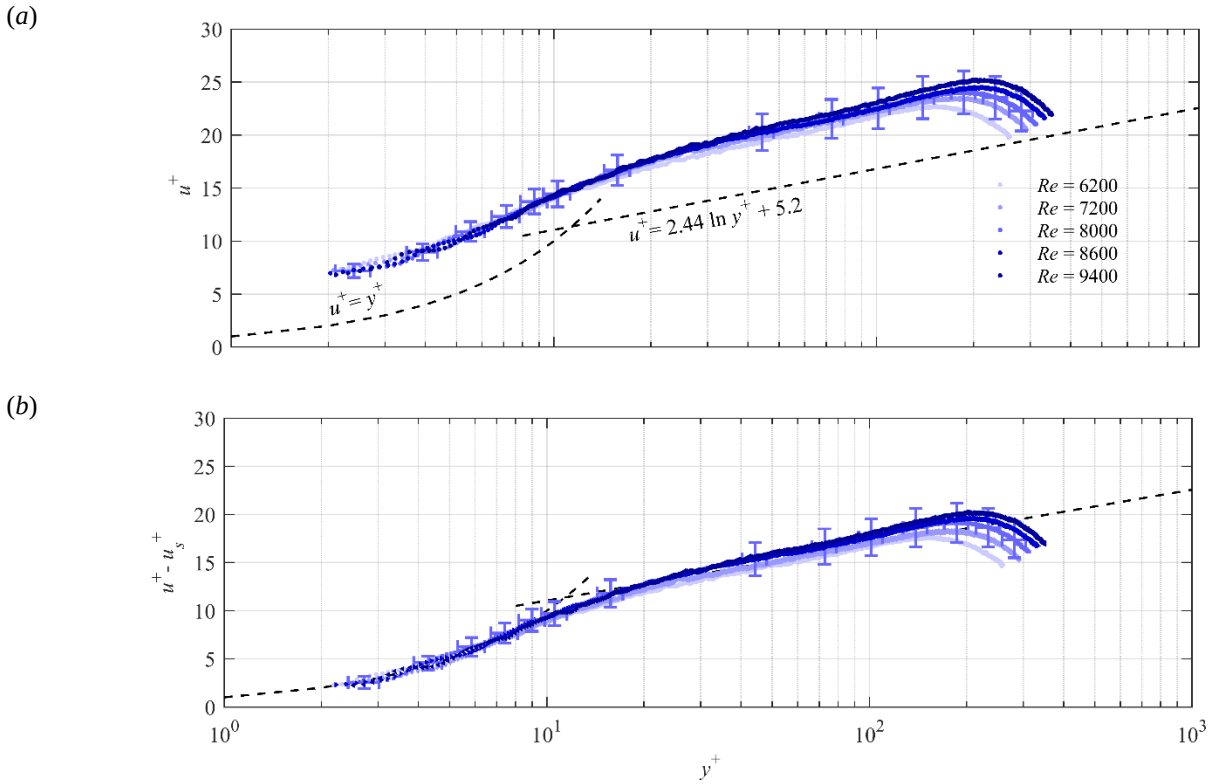


Figure 10 Semi-logarithmic profiles of (*a*) mean streamwise velocity at different *Re* over the SHS. (*b*) Semi-logarithmic profile of mean streamwise velocity when slip velocity is subtracted.

Similar to turbulent flow over a smooth surface, the analysis shows that, at different *Re*, normalized mean velocity profiles over an SHS overlap if the normalized slip velocity remains constant. For the moderate DR of the current experiment, the mean velocity profile of turbulent wall flows over an SHS still follows a log-law with von Kármán constant of $\kappa = 0.41$ (i.e. similar slope). However, the intercept of the logarithmic profile should be modified as $B + u_s^+$.

An estimation of the DR based on the difference between the wall shear stresses of the smooth surface and the SHS is shown in table 2. With increasing *Re*, DR increases slightly from 37% to 42%. The DR over the SHS was also directly measured using pressure drop measurements according to $DR_{dp} = 2.16 \times (dp_0 - dp)/dp_0$. Here, $dp_0$ and $dp$ are the pressure drop measurements over the smooth and SHS, respectively. The factor 2.16 is included since the SHS covers 46% of the channel surface area between the two pressure ports. The uncertainty of $DR_{dp}$ is estimated by applying error propagation theory to the 2% uncertainty in the pressure drop measurement and are presented in table 2. The pressure drop measurement underestimates DR by ~4% with respect to the DR estimated based on wall shear stress. However, $DR_{dp}$ also increases with increasing *Re*. It is worth mentioning that the two pressure ports also include two transitional regions, from no-slip to partial slip and the reverse. This affects the agreement of the results with respect to 2D-PTV.

Rastegari & Akhavan (2015) obtained an analytical equation for the DR, based on the original formulation of Fukagata *et al*. (2002), that decomposes DR into a term due to the direct effect of slip velocity($U_s/U_b$) and a second term due to turbulence modification. In the current investigation, $U_s/U_b$ reduces by 3% with an increase of *Re*. Thus, the increase in DR is associated with larger turbulence attenuation at higher *Re*. The contribution of turbulence attenuation to DR varies from 8 to 18% with increasing *Re*.

### 3.3 Reynolds stress over the SHS

All the non-zero components of the Reynolds stress tensor, $\langle u_i u_j \rangle$, for the turbulent flow over the SHS were measured by 3D-PTV. The profiles are normalized by $U_b$ of the lowest *Re* and shown in figure 11(*a*, *c*, *e*, *g*), while in figure 11(*b*, *d*, *f*, *h*), the profiles are normalized by the inner scales of each case. For ease of comparison, Reynolds stress profiles for the smooth surface are repeated in figure 11.

In figure 11(*a*), for each *Re*, the $\langle u^2 \rangle_b$ of the SHS is larger than the smooth surface in the immediate vicinity of the wall ($y < 0.01H$). However, with increasing wall-normal distance, $\langle u^2 \rangle_b$ of the SHS becomes smaller at the peak region. This trend is related to the effect of partial-slip at the wall, which intensifies the near-wall velocity fluctuations but attenuates turbulence farther away from the wall (Min & Kim 2004). For all *Re*, the peak of $\langle u^2 \rangle_b$ over the SHS is smaller than the peaks of $\langle u^2 \rangle_b$ of the smooth surface. This trend was also observed in the numerical simulations of Min & Kim (2004) and Busse & Sandham (2012) and the experiments of Ling (2017) and Abu Rowin & Ghaemi (2019) when they normalized $\langle u^2 \rangle$ for both the SHS and the smooth surface using a common scaling (the friction velocity of the no-slip surface). Farther away at $y/H > 0.06$, $\langle u^2 \rangle_b$ of the SHS is comparable with that over smooth surface for the smaller *Re* cases.

The Reynolds stress profiles normalized using the corresponding friction velocity results in larger $\langle u^2 \rangle^+$ for the SHS compared with the normalized Reynolds stresses of the smooth surface, as shown in figure 11(*b*). This is mainly because the friction velocity of the SHS is smaller than the friction velocity of the smooth surface at the same *Re* (see table 2). The $\langle u^2 \rangle^+$ of the SHS appears to gradually approach $\langle u^2 \rangle^+$ of the smooth surface with increasing $y^+$. A similar trend is observed for $\langle u^2 \rangle^+$ in the numerical simulations of Rastegari & Akhavan (2015). The simulation of Seo & Mani (2018) and the experiments of Ling et al. (2016) and Abu Rowin & Ghaemi (2019) also reported a larger $\langle u^2 \rangle^+$ over the SHS in the near-wall region, which gradually reduced and reached that of the smooth surface with increasing wall-normal distance. However, the new observation from the current data is that the $\langle u^2 \rangle^+$ profiles of SHS at different *Re* overlap when normalization by inner scaling is applied.

The $\langle v^2 \rangle_b$ profiles of the SHS are smaller than those of the smooth surface throughout the measurement domain in figure 11(*c*). A similar trend is observed in the DNS of Min & Kim (2004) for a flat surface with an imposed slip, and in the 2D-PTV measurement of Abu Rowin *et al.* (2017) over an SHS with a low roughness of $k^+ = 0.11$. However, experiment of Ling *et al*. (2016) reported a larger $\langle v^2 \rangle$ at the wall due to the large roughness of their SHSs. At higher *Re* in figure 11(*c*), a larger reduction of $\langle v^2 \rangle_b$ for the SHS is observed relative to that of the smooth surface. In figure 11(*d*), when inner scaling is applied, $\langle v^2 \rangle^+$ profiles for the SHS at all *Re* cases overlap. The overlapped profiles are higher than those of the smooth surface.

In the vicinity of the wall ($y < 0.02H$) in figure 11(*e*), a large $\langle w^2 \rangle_b$ is observed for the SHS relative to the smooth surface. This is associated with the slip velocity in the *z*-direction (Min & Kim 2004; Abu Rowin & Ghaemi 2019). Farther away from the wall, $\langle w^2 \rangle_b$ of the SHS becomes smaller than $\langle w^2 \rangle_b$ of the smooth surface. For all *Re* in figure 11(*f*), the $\langle w^2 \rangle^+$ profiles of the SHS are larger than the $\langle w^2 \rangle^+$ of smooth surface. This is consistent with DNS of Rastegari & Akhavan (2015). The 3D-PTV of Abu Rowin & Ghaemi (2019) also showed a larger $\langle w^2 \rangle^+$ in the inner layer. Figure 11(*f*) shows overlap of $\langle w^2 \rangle^+$ profiles for all *Re* cases.

In figure 11(*g*), at $y < 0.02H$ for all *Re* cases, $\langle uv \rangle_b$ of the SHS is larger than that of the smooth surface. As discussed by Abu Rowin *et al*. (2017), the increase of $\langle uv \rangle_b$ at the wall is a function of the surface roughness. Farther away from the wall, $\langle uv \rangle_b$ of the SHS is similar to the smooth surface for the smaller *Re* of 6200 and 7200. However, the higher *Re* cases, $\langle uv \rangle_b$ of the SHS is significantly smaller than the smooth surface. This reduction shows larger turbulence attenuation due to the slip velocity at higher *Re*.

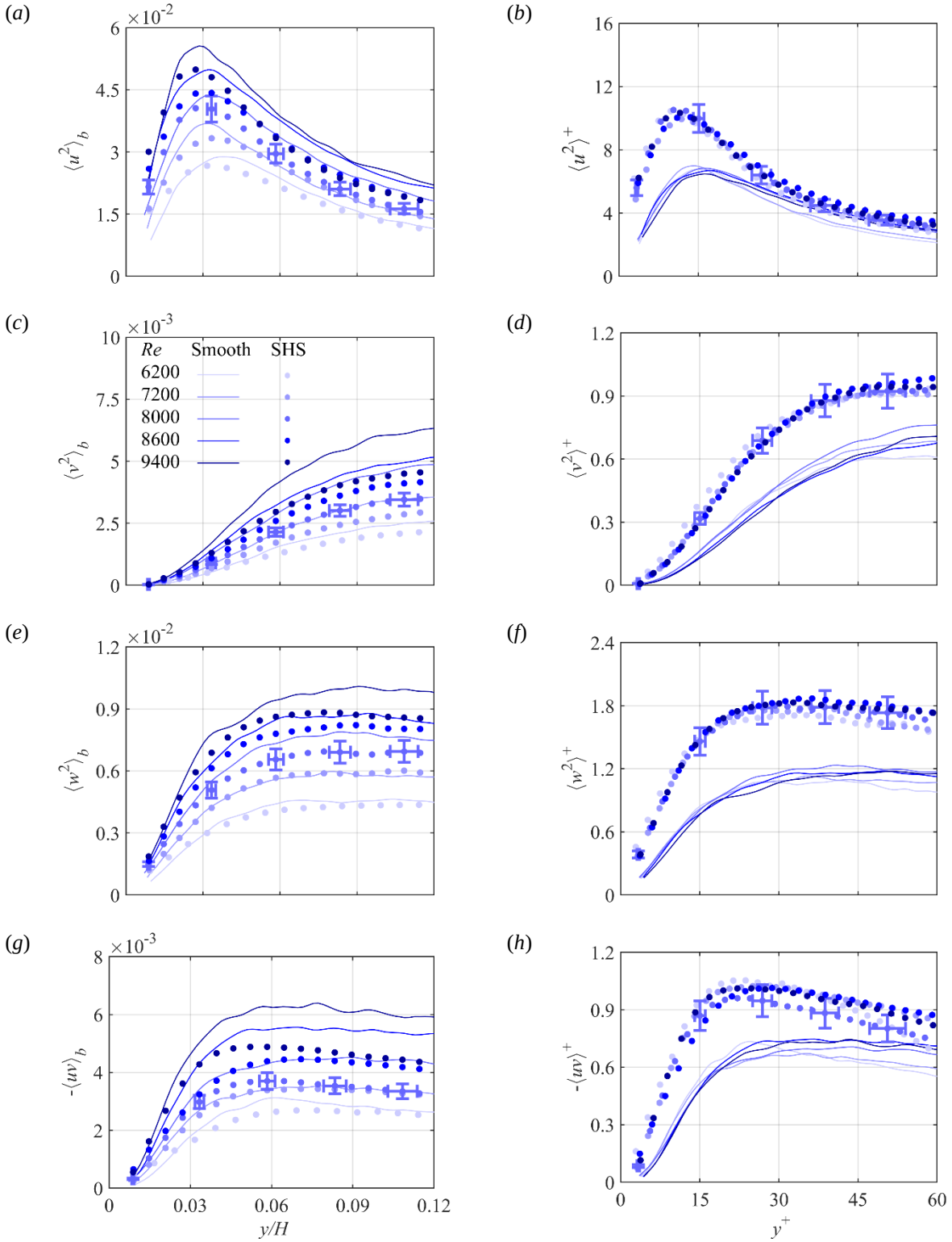


Figure 11 3D-PTV measurements of (*a*-*b*) streamwise, (*c*-*d*) wall-normal, (*e*-*f*) spanwise, and (*g*-*h*) shear Reynolds stresses over the smooth and SHS. The parameters of the left side plots are normalized by $U_b$ at the lowest *Re* and the channel height, while the parameters of right-side plots are normalized by their corresponding inner scaling.

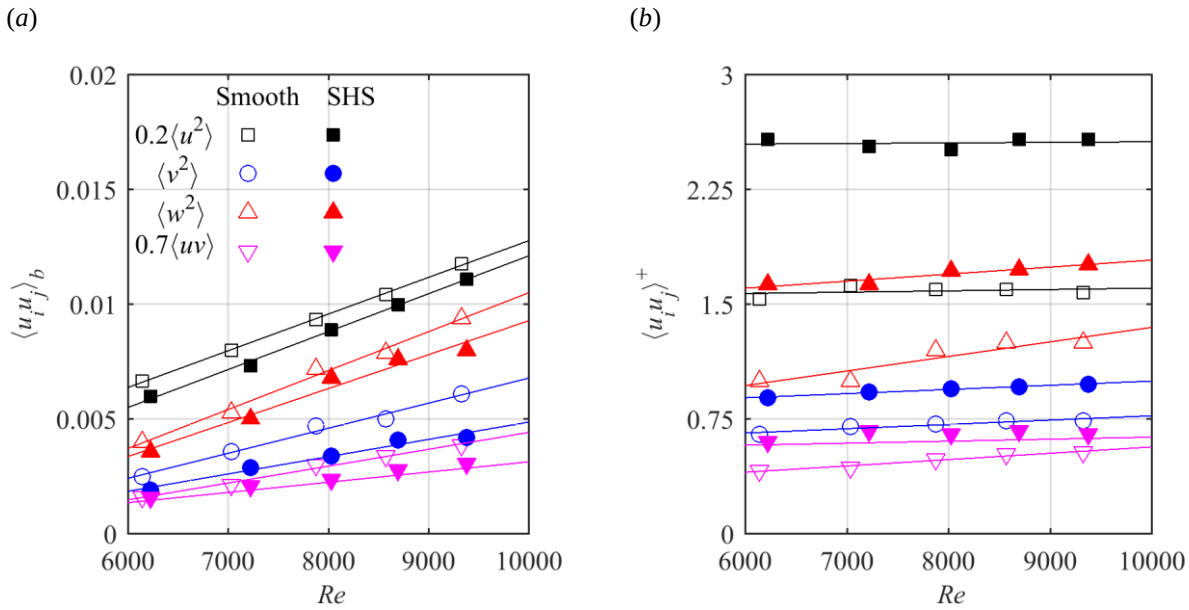


Figure 12 Maximum values of the Reynolds stresses from 3D-PTV measurement over the smooth and the SHS obtained from figure 11. The Reynolds stresses are non-dimensionalized by (*a*) $U_b$ of the lowest *Re* and (*b*) the corresponding $u_\tau$. For clarity, the $\langle u^2\rangle$ and $\langle uv\rangle$ profiles are multiplied by 0.2 and 0.7, respectively. The solid lines are linear fits.

The profiles of $\langle uv\rangle^+$ over the SHS are larger than those of the smooth surface in figure 11(*h*). The digital holographic microscopy of Ling *et al.* (2016) and the 3D-PTV of Abu Rowin & Ghaemi (2019) also reported a larger $\langle uv\rangle^+$ for the SHS compared with $\langle uv\rangle^+$ of the smooth surface. However, $\langle uv\rangle^+$ of Rastegari & Akhavan (2015) in figure 11(*h*) reported smaller $\langle uv\rangle^+$ profile for the SHS in comparison with $\langle uv\rangle^+$ of the smooth surfaces. The discrepancy can be associated with the roughness of the surfaces tested by Ling *et al.* (2016) and Abu Rowin & Ghaemi (2019) relative to the flat SHS modelled in DNS of Rastegari & Akhavan (2015). Again, an overlap of $\langle uv\rangle^+$ profiles for all *Re* near the wall is observed in figure 11(*h*).

The maximum values of the $\langle u_i u_j\rangle_b$ profiles for the SHS and the smooth surface at $y^+ < 50$ are plotted in figure 12(*a*) as a function of *Re*. For $\langle u^2\rangle$ and $\langle uv\rangle$, the maximum is the local peak of the profiles, but for $\langle v^2\rangle$ and $\langle w^2\rangle$ the maximum values belong to the data point farthest away from the wall. Fitted lines are added to figure 12 to demonstrate the overall trends. As can be seen, $\langle u_i u_j\rangle_b$ of both the smooth and SHS increases linearly with increasing *Re*. However, with the exception of $\langle u^2\rangle_b$, the linear fit for the SHS has a smaller slope compared with that of the smooth surface, resulting in a widening gap between $\langle u_i u_j\rangle_b$ of the SHS and that of the smooth surface with increasing *Re*. Therefore, at higher *Re*, the SHS has a larger effect on $\langle v^2\rangle_b$, $\langle w^2\rangle_b$, $\langle uv\rangle_b$. The maximum values of $\langle u_i u_j\rangle^+$ presented in figure 12(*b*) show that all the peak values of normalized Reynolds stresses over the SHS are higher than those of the corresponding smooth surface, and the variation with *Re* is negligible.

To scrutinize the effect of *Re* on the Reynolds stresses at the wall, the first data point from the 3D-PTV measurements at $y^+ \approx 4$ is plotted in figure 13 for both normalizations; using $U_b$ and $u_\tau$. In figure 13(*a*), $\langle u_i u_j\rangle_b$ over the smooth surface increases linearly with *Re*. Over the SHS, $\langle u_i u_j\rangle_b$ for all Reynolds stresses is larger than that of the smooth surface, and also follows a linear trend with increasing *Re*. The slope of the trend lines for the SHS are larger than those of the smooth surface, indicating a faster increase of SHS Reynolds stresses in the vicinity of the wall with increasing *Re*. In figure 13(*b*), for both the SHS and smooth surface, $\langle u_i u_j\rangle^+$ remains relatively constant with increasing *Re*. The $\langle u_i u_j\rangle^+$ values of SHS are also larger than the smooth surface at all *Re* cases.

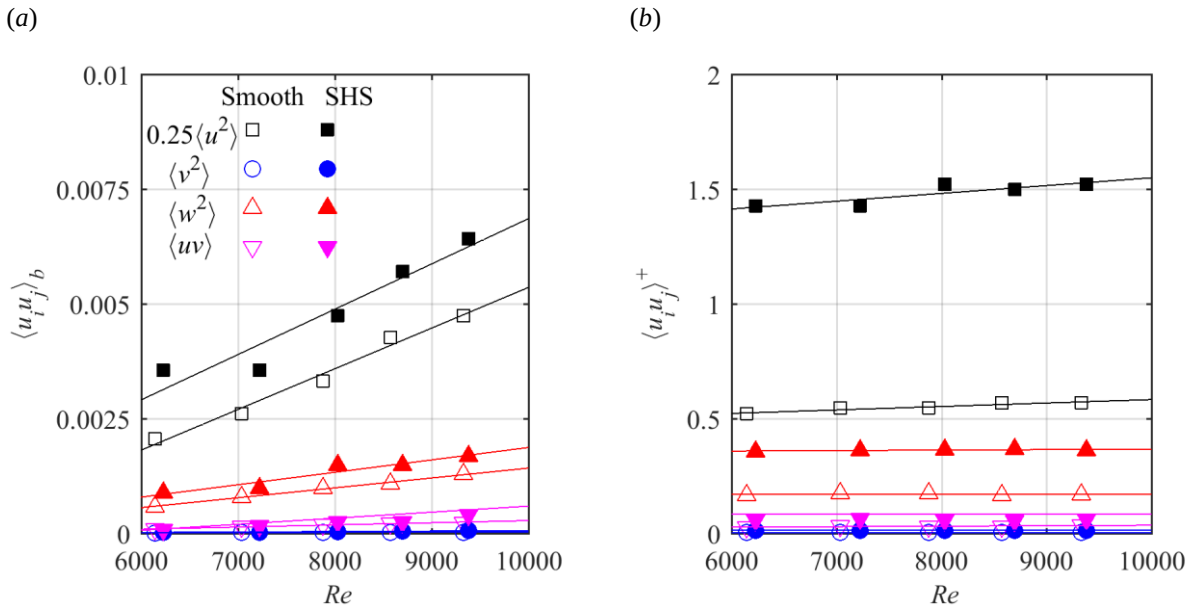


Figure 13 Reynolds stresses at $y^+ \approx 4$ from the 3D-PTV measurements over the smooth and SHS (obtained from figure 11) non-dimensionalized by (*a*) $U_b$ at the lowest *Re* and (*b*) the corresponding $u_\tau$. For clarity, the $\langle u^2\rangle$ profile is multiplied by 0.25. The solid lines are linear fits.

The above analysis, based on figures 11-13, provides a comparison of Reynolds stress profiles for SHS and smooth surfaces. In the vicinity of the wall, all the Reynolds stress components of a SHS in physical units (i.e. dimensional) are larger than those near a smooth surface. The increase of $\langle u^2\rangle$ and $\langle w^2\rangle$ is associated with the slip boundary condition, while the larger $\langle v^2\rangle$ and $\langle uv\rangle$ is due to roughness of an SHS. With increasing wall-normal distance, the Reynolds stresses of the SHS become smaller than those of the smooth surface. This is in general due to the attenuation of turbulence by the partial-slip at the wall. With increasing *Re*, the differences between the SHS and smooth surface become larger. At farther distances from the wall, the Reynolds stresses of the SHS and smooth surface converge. In contrast, when Reynolds stresses are normalized with the inner scaling, they overlap for all the five *Re* cases. The normalized Reynolds stresses are also larger than the normalized Reynolds stresses of the smooth surface. This observation is in spite of the smaller $Re_\tau$ of the SHS cases. Therefore, assuming a fixed $Re_\tau$, the turbulent flow over an SHS has larger normalized Reynolds stresses relative to those of a smooth surface. The larger normalized Reynolds stresses suggests that drag reduction caused by an SHS is mainly due to the direct effect of the slip velocity on the mean velocity gradient at the wall.

## 4 Conclusion

We presented an experimental investigation of the effect of the Reynolds number, *Re*, on the slip boundary condition and Reynolds stresses over a superhydrophobic surface (SHS). The friction Reynolds number, $Re_\tau$, of the smooth surface varied from 200 to 283, based on the friction velocity and the half-channel height. The SHS had a random pattern generated by spray coating. The root-mean-square of the surface roughness normalized by the wall-unit varied from 0.26 to 0.35. Two-dimensional particle tracking velocimetry (2D-PTV) was used to measure slip velocity, slip length, and the inner scaling of the turbulent flow over the SHS. Three-dimensional PTV (3D-PTV) was performed to investigate the effect of a *Re* change on all Reynolds stress components over the SHS.

A non-zero velocity was detected at the SHS wall for all *Re* cases, which increased linearly from 0.25 to 0.34 m/s with increasing *Re*. The results also showed that the slip length of the SHS reduced from 97.5 to 69.6 μm with increasing *Re*. In contrast, it was found that the change of *Re* had a negligible effect on slip velocity and slip length, when these parameters were normalized using inner scaling.

The scaling of the mean velocity profile for the SHS was investigated. At different *Re*, normalized mean velocity profiles over the SHS overlapped. In addition, the mean velocity profile of the turbulent wall flow followed the log-law, similar to that of the smooth surface. However, the intercept of the logarithmic profile was increased by an amount equal to the normalized slip velocity.

In the immediate vicinity of the wall, the streamwise and the spanwise Reynolds stresses were larger than the Reynolds stresses of the no-slip surface. However, farther away from the wall, the Reynolds stresses were smaller than those of the smooth surface, indicating turbulence attenuation. In contrast, when the Reynolds stresses were normalized using the corresponding friction velocity, the normalized Reynolds stresses overlapped for the investigated range of *Re*. The Reynolds stresses normalized using friction velocity were larger than the normalized Reynolds stresses of the no-slip surface.

## Appendix A. Uncertainty analysis

The major sources of uncertainty for the current 2D-PTV and 3D-PTV systems are due to the error in detecting particle peak location and estimating the wall location. The error of the particle peak detection is approximately 0.1 pixels, which results in an instantaneous velocity uncertainty of $\varepsilon_U$ = 8 mm/s for the 2D-PTV. As shown by Abu Rowin & Ghaemi (2019) using pre-multiplied linear spectral density analysis for a similar 3D-PTV system, the error for the streamwise and spanwise components (in-plane) is 0.1 pix, while the error for the wall-normal velocity (out-of-plane component) is 0.2 pix. This is equivalent to $\varepsilon_U = \varepsilon_w$ =14 mm/s for *U* and *W*, and $\varepsilon_V$ =28 mm/s for the *V* component.

As discussed in section 2.2, the uncertainty of estimating the wall location in the 2D-PTV is 25 μm ($\varepsilon_y$), which results in 5 mm/s uncertainty in the estimated friction velocity, $\varepsilon_{u_\tau}$. The error in estimating the wall location by applying the MART algorithm to the 3D-PTV images is approximately 1 pix, which results in $\varepsilon_y$ of 35.5 μm.

The uncertainty of the normalized mean streamwise velocity $\varepsilon_{U^+}$ is estimated based on the error propagation theory as

$$\varepsilon_{U^+} = |U^+| \cdot \sqrt{\left(\frac{\varepsilon_U}{U}\right)^2 + \left(\frac{\varepsilon_{u_\tau}}{u_\tau}\right)^2}. \tag{A1}$$

The uncertainty in the normalized wall-normal location $\varepsilon_{y^+}$ is also given as

$$\varepsilon_{y^+} = |y^+| \cdot \sqrt{\left(\frac{\varepsilon_y}{y}\right)^2 + \left(\frac{\varepsilon_{u_\tau}}{u_\tau}\right)^2}. \tag{A2}$$

The uncertainty of normalized Reynolds stresses can be estimated as

$$\varepsilon_{\langle u_i u_j \rangle^+} = \left|\langle u_i u_j \rangle^+\right| \sqrt{\left(\frac{\varepsilon_{\langle u_i u_j \rangle}}{\langle u_i u_j \rangle}\right)^2 + \left(\frac{2\varepsilon_{u_\tau}}{u_\tau}\right)^2}. \tag{A3}$$

The measurement uncertainty was estimated for the *Re* = 8000 case based on the above equations, and was indicated as error bars in figure 4, 5, 6, 7, 10, and 11.

## Data availability

The data that supports the findings of this study are available within the article and from the corresponding author upon reasonable request.

## Acknowledgement

The authors are grateful for the financial support of the Natural Sciences and Engineering Research Council of Canada (RGPIN-2014-04320).

## References

Abu Rowin, W., Hou, J. & Ghaemi, S. 2017 Inner and outer layer turbulence over a superhydrophobic surface with low roughness level at low Reynolds number. Phys. Fluids. **29**(9), 095106.

Abu Rowin, W. & Ghaemi, S. 2019 Streamwise and spanwise turbulence structures over superhydrophobic surfaces. J. Fluid Mech. 870, 1127-1157.

Aljallis, E., Sarshar, M., Datla, R., Sikka, V. & Jone, A. 2013 Experimental study of skin friction drag reduction on superhydrophobic flat plates in high Reynolds number boundary layer flow. Phys. Fluids. **25**, 025103.

Bidkar, R., Leblanc, L., Kulkarni, A., Bahadur, V., Ceccio, S. & Perlin, M. 2014 Skin-friction drag reduction in the turbulent regime using random-textured hydrophobic surfaces. Phys. Fluids. **26**, 085108.

Busse, A. & Sandham, N. 2012 Influence of an anisotropic slip-length boundary condition on turbulent channel flow. Phys. Fluids. **24**, 055111.

Cassie, A. & Baxter, S. 1944. On the criteria for reverse transition in a two-dimensional boundary layer flow. Trans. Faraday Soc.

Ceccio, S. 2010. Friction drag reduction of external flows with bubble and gas injection. Annual Review of Fluid Mechanics. **42**, 183-203.

Clauser, F. 1956 The turbulent boundary layer. In Advances in applied mechanics. **4**, 1-51.

Daniello, R., Waterhouse, N. & Rothstein, J. 2009 Drag reduction in turbulent flows over superhydrophobic surfaces. Phys. Fluids. **21**(8), 085103.

Dean, R. 1978 Reynolds number dependence of skin friction and other bulk flow variables in two-dimensional rectangular duct flow. Trans. ASME J. Fluids Eng. **100** (2), 215-223.

Dilip, D., Jha, N., Govardhan, R. & Bobji, M. 2014 Controlling air solubility to maintain "Cassie" state for sustained drag reduction. Colloids and Surfaces A: Physicochemical and Engineering Aspects. **459**, 217-224.

Elsinga, G., Scarano, F., Wieneke, B. & Van Oudheusden, B. 2006 Tomographic particle image velocimetry. Exp. Fluids. **41**(6), 933-947.

George, W. 2013. Lectures in Turbulence for the 21st Century. Chalmers University of Technology.

Gogte, S., Vorobieff, P., Truesdell, R., Mammoli, A., Van Swol, F., Shah, P. & Brinker, C. 2005. Effective slip on textured superhydrophobic surfaces. Physics of fluids. **17**(5), 051701.

Gose, J., Golovin, K., Boban, M., Mabry, J., Tuteja, A., Perlin, M. & Ceccio, S. 2018 Characterization of superhydrophobic surfaces for drag reduction in turbulent flow. J. Fluid Mech. **845**, 560-580.

Gupta, R., Vaikuntanathan, V. & Sivakumar, D. 2016 Superhydrophobic qualities of an aluminum surface coated with hydrophobic solution NeverWet. Colloids and Surfaces A: Physicochemical and Engineering Aspects. **500**, 45-53.

Jung, Y. & Bhushan, B. 2009. Biomimetic structures for fluid drag reduction in laminar and turbulent flows. Journal of Physics: Condensed Matter. **22**(3), 035104.

Lee, J., Jelly, T. & Zaki, T. 2015. Effect of Reynolds number on turbulent drag reduction by superhydrophobic surface textures. Flow, Turbulence and Combustion. **95**(2-3), 277-300.

Lee, M. & Moser, R. 2015. Direct numerical simulation of turbulent channel flow up to $Re_\tau \sim 5200$. Journal of Fluid Mechanics, 774, 395-415.

Ling, H. 2017 Experimental investigation of friction drag reduction in turbulent boundary layer by super-hydrophobic surfaces. Doctoral dissertation, Johns Hopkins University.

Ling, H., Srinivasan, S., Golovin, K., Mckinley, G., Tuteja, A. & Katz, J. 2016 High-resolution velocity measurement in the inner part of turbulent boundary layers over super-hydrophobic surfaces. J. Fluid Mech. **801**, 670-703.

Ling, H., Katz, J., Fu, M. & Hultmark, M. 2017 Effect of Reynolds number and saturation level on gas diffusion in and out of a superhydrophobic surface. Phys. Rev. Fluids. **2**(12), 124005.

Liu, C., Liao, S., Song, J., Mauk, M., Li, X., Wu, G., Ge, D., Greenberg, R., Yang, S. & Bau, H. 2016 A high-efficiency superhydrophobic plasma separator. Lab on a Chip. **16**(3), 553-560.

Martell, M., Rothstein, J. & Perot, J. 2010 An analysis of superhydrophobic turbulent drag reduction mechanisms using direct numerical simulation. Phys. Fluids. **22**, 065102.

Meinhart, C., Wereley, S. & SANTIAGO, J.G. 2000 A PIV algorithm for estimating time-averaged velocity fields. J. Fluids Eng. **122**(2), 285-289.

Min, T. & Kim, J. 2004 Effects of hydrophobic surface on skin-friction drag. Phys. Fluids. **16**, L55-L58.

Rastegari, A. & Akhavan, R. 2015 On the mechanism of turbulent drag reduction with superhydrophobic surfaces. J. Fluid Mech. **773**, R4.
Reholon, D. & Ghaemi, S. 2018 Plastron morphology and drag of a superhydrophobic surface in
turbulent regime. Phys. Rev. Fluids. **3**, 104003.
Rothstein, J. 2010 Slip on superhydrophobic surfaces. Annu. Rev. Fluid Mech. **42**, 89-109.
Park, H., Sun, G. & Kim, C. 2014 Superhydrophobic turbulent drag reduction as a function of surface grating parameters. J. Fluid Mech. **747**, 722-734.
Peguero, C. & Breuer, K. 2009. On Drag Reduction in Turbulent Channel Flow over Superhydrophobic Surfaces. In Springer Proceedings in Physics. 233-236.
Schanz, D., Gesemann, S., Schröder, A., Wieneke, B. & Novara, M. 2012. Non-uniform optical transfer functions in particle imaging: calibration and application to tomographic reconstruction. Measurement Science and Technology. **24**(2), 024009.
Schanz, D., Gesemann, S. & Schröder, A. 2016 Shake-The-Box: Lagrangian particle tracking at high particle image densities. Exp. Fluids. **57**(5), 70.
Seo, J. & Mani, A. 2018 Effect of texture randomization on the slip and interfacial robustness in turbulent flows over superhydrophobic surfaces. Phys. Rev. Fluids. **3**(4), 044601.
Srinivasan, S., Kleingartner, J., Gilbert, J., Cohen, R., Milne, A. J. & Mckinley, G. 2015 Sustainable drag reduction in turbulent Taylor-Couette flows by depositing sprayable superhydrophobic surfaces. Phys. Rev. Letters. **114**(1), 014501.
Vajdi Hokmabad, B. & Ghaemi, S. 2017 Effect of flow and particle-plastron collision on the longevity of superhydrophobicity. Scientific Reports. **7**, 41448.
Vinuesa, R., Noorani, A., Lozano-Durán, A., Khoury, G., Schlatter, P., Fischer, P. & Nagib, H. 2014. Aspect ratio effects in turbulent duct flows studied through direct numerical simulation. Journal of Turbulence, **15**(10), 677-706.
Wieneke, B. 2008 Volume self-calibration for 3D particle image velocimetry. Exp. Fluids. **45**(4), 549-556.
Woolford, B., Prince, J., Maynes, D. & Webb, B. 2009 Particle image velocimetry characterization of turbulent channel flow with rib patterned superhydrophobic walls. Phys. Fluids. **21**, 085106.
Zhao, J., Du, X. & Shi, X. 2007. Experimental research on friction-reduction with super-hydrophobic surfaces. Journal of Marine Science and Application. **6**(3), 58-61.